

Wavelet analysis of the cosmic web formation

J. Einasto^{1,2,3}, G. Hütsi¹, E. Saar^{1,2}, I. Suhhonenko¹, L. J. Liivamägi¹, M. Einasto¹, V. Müller⁴, A. A. Starobinsky^{5,6}, E. Tago¹, and E. Tempel¹

¹ Tartu Observatory, EE-61602 Tõravere, Estonia

² Estonian Academy of Sciences, EE-10130 Tallinn, Estonia

³ ICRA Net, Piazza della Repubblica 10, 65122 Pescara, Italy

⁴ Leibniz-Institut für Astrophysik Potsdam, An der Sternwarte 16, D-14482 Potsdam, Germany

⁵ Landau Institute for Theoretical Physics, Moscow 119334, Russia

⁶ Research Center for the Early Universe (RESCEU), Graduate School of Science, The University of Tokyo, Tokyo 113-0033, Japan

Received 4 November 2010/ Accepted 5 May 2011

ABSTRACT

Context. According to the modern cosmological paradigm, galaxies and galaxy systems form from tiny density perturbations generated during the very early phase of the evolution of the Universe.

Aims. Using numerical simulations, we study the evolution of the density perturbation phases of different scales to understand the formation and evolution of the cosmic web.

Methods. We apply the wavelet analysis to follow the evolution of high-density regions (clusters and superclusters) of the cosmic web.

Results. We show that the maxima and minima positions of density waves (their spatial phases) almost do not change during the evolution of the structure. Positions of density perturbation extrema of are more stable for large scale perturbations. In the context of the present study we call density waves of scale $\geq 64 h^{-1}$ Mpc large, waves of scale $\approx 32 h^{-1}$ Mpc medium, and waves of scale $\approx 8 h^{-1}$ Mpc small, within a factor of 2.

Conclusions. In the cosmic structure formation of the synchronisation (coupling) of density waves of different scales plays an important role.

Key words. cosmology: large-scale structure of the Universe; cosmology: early Universe; cosmology: theory; methods: numerical

1. Introduction

The basic structural elements of the Universe are filamentary superclusters and voids forming a web-like structure – the supercluster-void network (Einasto et al. 1980; Zeldovich et al. 1982; de Lapparent et al. 1986; Bond et al. 1996). The standard cosmological paradigm predicts that a period of accelerated expansion, dubbed inflation (Starobinsky 1980; Guth 1981; Linde 1982; Albrecht & Steinhardt 1982), generated density fluctuations (Mukhanov & Chibisov 1981; Hawking 1982; Starobinsky 1982; Guth & Pi 1982) as well as primordial gravitational waves (Starobinsky 1979) through quantum-gravitational processes. In the simplest form of this scenario, the primordial density field is predicted to form a statistically homogeneous, isotropic and almost-Gaussian random field, after the transition from quantum to approximate classical description of perturbations.

If the hypothesis of primordial Gaussianity is correct, then density waves of different scales began with random and uncorrelated spatial phases. As the density waves evolve, they interact with others in a non-linear way. This interaction leads to the generation of non-random and correlated phases which form a spatial pattern of the present cosmic web. Owing to non-linear processes during galaxy formation and the physical biasing problem (almost no galaxies form in low-density regions), the present density field is highly non-Gaussian. There have been a number of attempts to gain quantitative information on the behaviour of

phases in gravitational systems; for a review see Coles (2009) and references therein.

Using numerical simulations, Ryden & Gramann (1991) showed that initial phase information is rapidly lost in short wavelengths during evolution. Hikage et al. (2005) analysed the clustering of SDSS galaxies using the distribution function of the sum of Fourier phases. Fourier phases are statistically independent of the Fourier amplitudes, thus the phase statistics plays a complementary role to the conventional two-point statistics of galaxy clustering. Gaussian fields have a uniform distribution of the Fourier phases over $0 \leq \theta_k \leq 2\pi$. Therefore, characterising the correlation of phases is expected to be a direct means to explore non-Gaussian features. From the comparison of observations with mock catalogues constructed from N-body simulations, the authors find that the observed phase correlations for the galaxies agree well with those predicted by the spatially flat Λ CDM model, evolved from Gaussian initial conditions.

The analysis in Fourier space is, however, not sensitive to the location of particular high-density features in real space, such as filaments, clusters, and superclusters. To have a better understanding of the texture of the cosmic web, the web must be studied in the real space. Different statistical measures have been used to describe quantitatively the cosmic texture, for recent reviews see Martínez & Saar (2002), Saar (2009), and van de Weygaert & Schaap (2009).

One of these statistics is the wavelet analysis, which analyses properties of waves of various scales in real space (see Jones 2009, and references therein). Wavelet analysis has been used to

Send offprint requests to: J. Einasto, e-mail: einasto@aai.ee

detect voids and filaments in the Center for Astrophysics (CfA) survey first slice (Slezak et al. 1993), to de-noise the galaxy distribution (Martínez et al. 2005), to detect the integrated Sachs-Wolfe effect in the cosmic microwave background (CMB) radiation (Vielva et al. 2006), to study the discreteness effects in simulations (Romeo et al. 2008), and for many other purposes where the spatial position of structural elements is important.

The goal of this paper is to investigate the evolution of the texture of the cosmic web. It is well known that on small scales the original phase information is lost during the non-linear stage of the evolution (Ryden & Gramann 1991). On the other hand, the main large-scale skeleton of the texture of the cosmic web is already determined by the initial gravitational potential field (Kofman & Shandarin 1988). If considered from the point of view of the Fourier decomposition, maxima and minima in *any* spatial distribution occur in the points where phases of the Fourier modes are synchronised. However, there is a non-trivial problem, which is not completely solved yet.

In the classical “down-top” model, like the isocurvature model, there are no built-in large-scale features. The structure formation starts from small-scale systems, which grow by random clustering. In the classical “top-down” model, like the adiabatic neutrino-dominated hot dark matter model, there is a built-in cut-off scale, which determines the scale of the structure. The presently accepted dark energy dominated Λ CDM model is essentially a “down-top” model, because the structure formation starts from small systems. This model differs from the classical “down-top” model in one important detail – here a broad power spectrum of density perturbations is present. Objects of a smaller scale and mass form earlier. But in the case of a broad power spectrum of perturbations, it becomes a non-trivial question whether extrema of perturbations of a given scale will remain at the same places if perturbations of larger scales are added. This may occur only if some phase synchronisation or coupling between perturbations of *different scales* exists. In the case of the broad wave spectrum, extrema of density perturbations should define locations where gravitationally bound objects and voids form first. On the other hand, the gravitational potential defines the location of the skeleton of the cosmic web knots. Consequently, it is not clear at all why extrema of density perturbations coincide with knots defined by the gravitational potential. In other words: Why is the skeleton stable in the “down-top” Λ CDM model? As we see in this paper, just because of this synchronisation between waves of different scales.

Studies of Fourier phases show that the phase coupling in the non-linear regime plays an important role in the formation of the fine texture of the cosmic web (Chiang et al. 2002). To avoid complications caused by the highly non-linear regime, we concentrate on the evolution of waves at intermediate and large scales using the wavelet decomposition of the evolving density field. The Fourier modes are fully specified by their wavelength, their orientation, and phase. Because the phase determines where the maxima and minima are located along a Fourier mode, we also use the same terminology (somewhat less strict this time) once we speak about the wavelet decomposition of the density field. Here we assume that the (spatial) phase and the locations of the maxima and minima carry the same information, and thus will use these terms interchangeably in the following. Also, quite often the locations of the cells inside the cubical density grid are located as (i, j, k) , with i, j , and k are integers that run from 1 to N , where $N = 256$ is most often assumed throughout the work.

We shall focus our attention on the two main problems: the evolution of phases (positions of maxima) of density perturbations at medium and large scales, and the phase coupling (syn-

chronisation) of perturbations of different scales. To follow the evolution of perturbations of different size, we use simulations in boxes of various sizes from 100 to 768 h^{-1} Mpc. To find the sensitivity of our results to the resolution, we make simulations with 256^3 and 512^3 cells and equal number of particles. For comparison with the real Universe, we shall calculate the density field and its wavelet decompositions for a slice (wedge) of the Sloan Digital Sky Survey (SDSS). Preliminary results of this study have been reported at several conferences (Einasto 2006a,b, 2009). This paper is a follow-up of a study by Einasto et al. (2005) of the environmental effects of clusters in SDSS and simulations.

In the next section we describe the numerical models used in this study. We also make a qualitative wavelet analysis of the simulated density field, follow the density evolution in time, and compare the evolution of density waves of various scales. In Section 3 we make a correlation analysis of wavelet-decomposed density fields. In Section 4 we analyse the luminosity density field of the SDSS, and study the role of phase synchronisation in the formation of clusters and superclusters. In Section 5 we discuss our results. The last section gives our main conclusions.

2. Qualitative wavelet analysis of the cosmic web evolution

2.1. Modelling the cosmic web evolution

In order to understand the evolution of the supercluster-void phenomenon, numerical simulations need to be performed in a box that contains both small- and large-scale waves. The most common systems of galaxies are groups and galaxy clusters with a characteristic scale of $\sim 1 h^{-1}$ Mpc, therefore the simulation must have at least a resolution of this scale. On the other hand, the largest non-percolating systems are superclusters, which have a characteristic scale up to $\sim 100 h^{-1}$ Mpc. Superclusters have a very different richness from small systems like the Local supercluster to very rich systems like the Shapley supercluster (Einasto et al. 2001). Clearly this variety has its origin in density perturbations of still larger scales. Thus, to understand the supercluster-void phenomenon correctly, the influence of very large-scale density perturbations should be studied, too.

To have both high spatial resolution and the presence of density perturbations in a broad interval of scales, we used in this analysis simulations in boxes of sizes 100 h^{-1} Mpc, 256 h^{-1} Mpc, and 768 h^{-1} Mpc, with the resolution of 256^3 particles and simulation cells; these models are designated as M100, M256 and M768, respectively. For simulations we used the AMIGA code (Knebe et al. 2001). This code uses an adaptive mesh technique in regions where the density exceeds a fixed threshold. For comparison we used a model of box size 256 h^{-1} Mpc with the resolution of 512^3 particles and cells, this model is designated L256. In the last case we used the GADGET code for simulations (Springel 2005). Results obtained from models with different resolution are very similar in the context of the present study, thus in the graphical representation of our results we mostly use models M100, M256, and M768. The model L256 has been used to find a catalogue of density field (DF) clusters of galaxies, to study the dependence of the mass of DF clusters on the density of the environment, and to compare wavelets of models with different cut-off scale (see Figure 8 below).

The initial density fluctuation spectrum was generated using the COSMICS code by Bertschinger (1995)¹. We assumed

¹ <http://arcturus.mit.edu/cosmics>

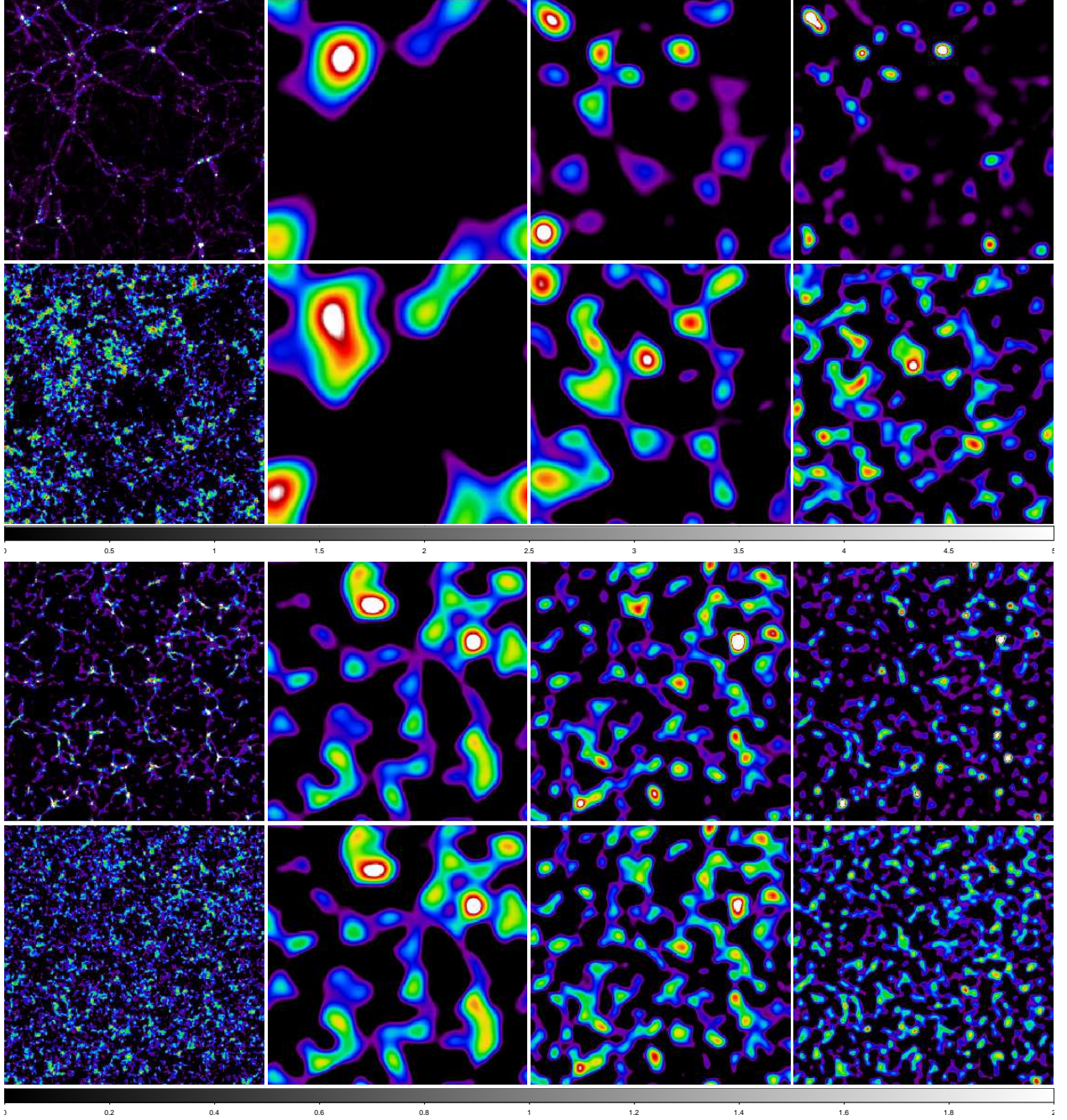


Fig. 1. High-resolution density fields and their wavelet decompositions for models M100 and M768, upper two and lower two rows, respectively. Model M100 fields are given at $k = 1$ coordinate, M768 fields at $k = 217$ coordinate. Left panels show the density fields, next panels their wavelet decompositions. For both models upper panels show the field and wavelets at redshift $z = 0$, and lower panels at redshift $z = 100$. For model M100 we show the wavelets w_6 , w_5 , and w_4 , for model M768 wavelets w_5 , w_4 , and w_3 . In plotting density fields and wavelets we use only over-dense regions: i.e., lower density limit (which corresponds to black level in DS9 colour palette SLS) is taken equal to 1 for the density field, and 0 for wavelets. Upper density levels (which correspond to white in palette SLS) are given in Table 1. Table 1 gives also the upper smoothing wavelength S_{wnd} in h^{-1} Mpc for all wavelets.

cosmological parameters $\Omega_m = 0.28$, $\Omega_\Lambda = 0.72$, $\sigma_8 = 0.84$, and the dimensionless Hubble constant $h = 0.71$; to generate the initial data we took the baryonic matter density $\Omega_b = 0.044$. Calculations started in an early epoch, $z = 500$. Particle positions and velocities were extracted for 13 epochs between redshifts $z = 100, \dots, 0$. In the present study we used only a part of these data, depending on the goal of the task.

2.2. Wavelet decomposition of simulated density fields

To see the effects of density waves of different scales and to understand the evolution of the density field, we shall use our models M100, M256, and M768. The density fields were calculated for all simulation epochs and were used to find the wavelets up to the level 6. The analysis was made in three dimensions. For illustrations of the results we use two-dimensional slices in i , j -coordinates through the simulation box at fixed

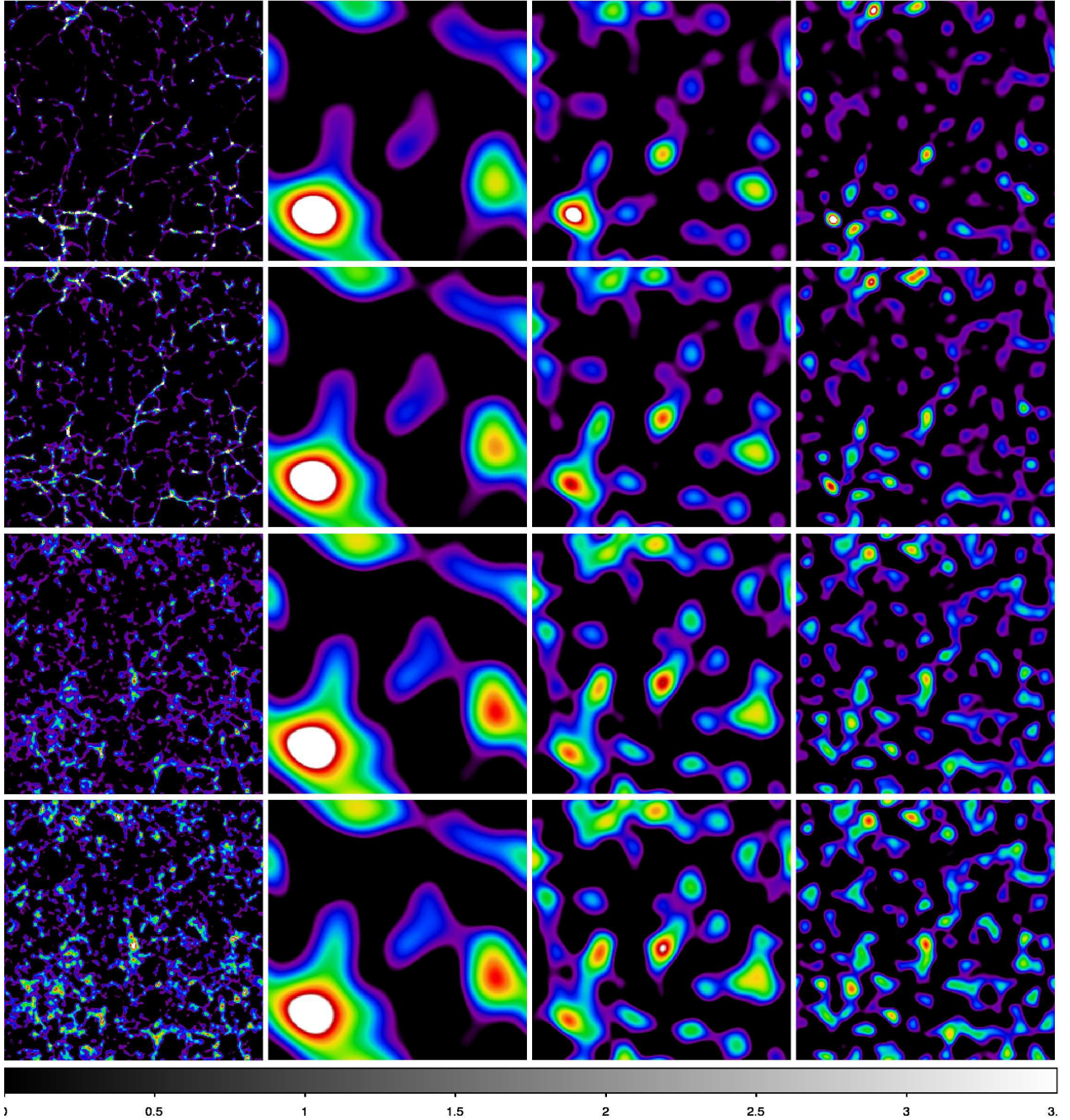


Fig. 2. High-resolution density field of the model M256 is shown in the left column, at $k = 153$ coordinate. The second, third, and fourth columns show the wavelet w_6 , w_5 , and w_4 decompositions at the same k , respectively. The upper row gives data for the present epoch, $z = 0$, the second row for redshift $z = 1$, the third row for redshift $z = 5$, and the last row for redshift $z = 10$. Densities are expressed in linear scale. Parameters used for plotting are given in Table 1.

k -coordinates. The calculation of wavelets is explained in Appendix A.3.

The evolution of waves in models M100 and M768 are shown in Fig. 1. High-resolution density fields at redshifts $z = 0$ and $z = 100$ are shown in the left panels of Fig. 1. The wavelet decompositions of these density fields are shown for the same slices in the following panels of the figure. We show three wavelet levels: w_6 , w_5 , and w_4 for the model M100; and w_5 , w_4 , and w_3 for the model M768. These wavelets show the evolution of large and intermediate scale waves. Upper smoothing wavelengths and upper density levels for plotting are given in Table 1. We note that the upper smoothing scale of a wavelet

w_n is equal to the kernel diameter, used in the calculation of the density field D_n , see Appendix A.3.

To see the evolution of the density field at intermediate time-steps we show in Fig. 2 the high-resolution density fields of the model M256 at four redshifts: $z = 10, 5, 1, 0$. Wavelet decompositions at levels w_6 , w_5 , and w_4 for the same redshifts are shown in the same Figure. Colour-coding of wavelets at different redshifts is chosen so that a certain colour approximately corresponds to the density level, corrected by the linear growth factor for that redshift. Parameters used for plotting are given in the Table 1.

Table 1. Parameters used in wavelet figures.

Model (1)	z (2)	DFu (3)	Dw6u (4)	Dw5u (5)	Dw4u (6)	Swnu (7)
M100	0	40	1.0	1.8	5.0	50
M100	100	1.15	0.0085	0.018	0.03	50
M256	0	20	0.55	1.5	3.5	128
M256	1	10	0.3	0.75	1.75	128
M256	5	4	0.09	0.2	0.45	128
M256	10	2	0.05	0.1	0.2	128
M768	0	10	0.25	0.86	2.0	192
M768	100	1.08	0.004	0.009	0.018	192

Notes.

- 1: Model;
- 2: Redshift z ;
- 3: Upper density limit of the high-resolution density field used in Figs. 1, 2;
- 4: Upper density limit of the wavelet w_6 (w_5 for the model M768) used in Figs. 1, 2;
- 5: Upper density limit of the wavelet w_5 (w_4) used in Figs. 1, 2;
- 6: Upper density limit of the wavelet w_4 (w_3) used in Figs. 1, 2;
- 7: Upper smoothing wavelength in h^{-1} Mpc of the largest wavelet Sw6u (Sw5u); the upper smoothing wavelength of the next wavelet Sw5u (Sw4u) is 2 times smaller than that of Sw6u (Sw5u), and that of Sw4u (Sw3u) is 4 times smaller than that of Sw6u (Sw5u). Lower smoothing wavelengths of all the wavelets are 2 times smaller than the upper ones.

2.3. The evolution of density waves in time

Let us first study the evolution of wavelets of various scales in time. It is well known that during the early stage of the evolution of the Universe the main evolution is in the growth of amplitudes of density perturbations. In the early stage of the evolution, the growth of amplitudes is almost linear.

How well this approximation works in our numerical simulations can be seen when we compare wavelets of different scales at various redshifts. The largest wavelets shown in Figs. 1 and 2 are w_6 for the models M100 and M256, and w_5 for the model M768. Upper smoothing scales of these largest wavelets are 50, 128, and 192 h^{-1} Mpc (models M100, M256, and M768, see Table 1). The upper smoothing scales of next level wavelets for these models are 25, 64, 96 h^{-1} Mpc. The upper smoothing scales of the lowest level wavelets, shown in Figs. 1 and 2 for models M100, M256, and M768, are 12.5, 32, and 48 h^{-1} Mpc, respectively. The upper smoothing scales of the wavelet w_1 are 1.56, 4, and 12 h^{-1} Mpc for these models.

A look at Figs. 1 and 2 shows that in the model M100 there are already considerable changes in positions and shapes of density configurations in the wavelet w_5 (upper smoothing scale 25 h^{-1} Mpc). In the model M256 changes of the wavelet w_5 (upper smoothing scale 64 h^{-1} Mpc) are still relatively small.

In the lowest scale wavelets (w_4 of the model M256) the patterns of density distributions at various epochs are still fairly similar, however, changes in positions and density levels are more visible. These scales are upper limits of wavelengths of given wavelets, lower limits are twice smaller. Thus the mean smoothing scale of the wavelet w_4 of the model M256 is $32/\sqrt{2} = 22.6 h^{-1}$ Mpc. Changes of patterns in the wavelet w_4 of the model M100 (mean smoothing scale 8.8 h^{-1} Mpc) are already fairly strong, both in the position and the density level.

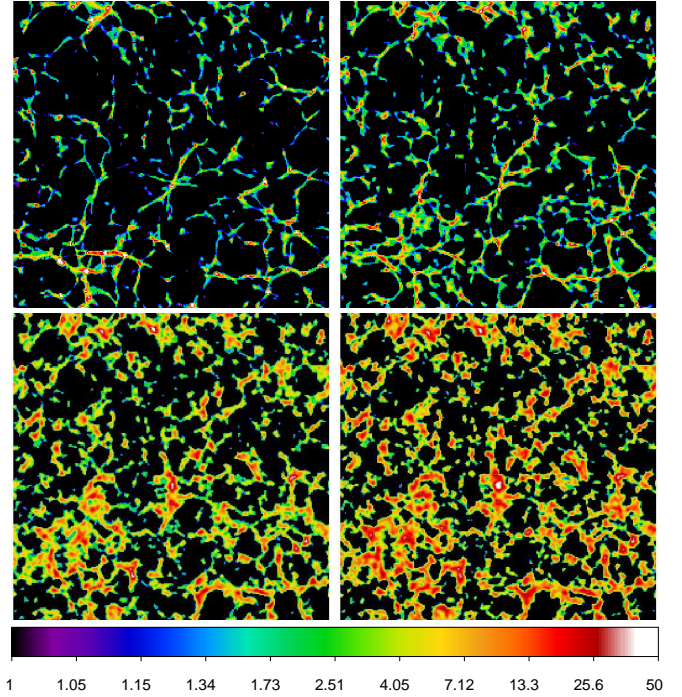


Fig. 3. Evolution of the high-resolution density field of the model M256, at $k = 153$ coordinate. Upper panels are for $z = 0$ and $z = 1$, lower panels for $z = 5$ and $z = 10$. The densities are expressed in the logarithmic scale; this allows to see better the evolution in low-density regions. Only over-densities are shown, i.e., lower density limit for plotting is taken 1. Upper densities for plotting with the DS9 package, corresponding to white, are 50, 25, 5, and 2.5 for redshifts 0, 1, 5, and 10, respectively. Colour codes shown at the bottom correspond to redshift $z = 0$ (upper left panel).

To see the evolution of the filamentary density field better, we show in Fig. 3 the high-resolution density field of the model M256 again, with densities expressed in a logarithmic scale. We use the same epochs and $k = 153$ coordinate as in Fig. 2. In the lower left region a very rich supercluster is located, visible in the wavelet w_6 of Fig. 2 as a large white area. The position of the supercluster does not change with time, the density contrast increases approximately proportional to the linear growth factor (used in setting colours for plotting). Most visible effects are the contraction of the filamentary system towards the centre of the supercluster, thinning of filaments, and merging of small filaments.

Our simple qualitative analysis shows that the evolution of waves of medium and large scales is approximately linear as expected. Positions of maxima of these waves change very little with time. Waves of smaller scales change their positions of maxima, this can be considered as phase shifts of maxima. The shift is larger for small-scale waves. These shifts are caused by two effects: the contraction of high-density regions (superclusters), and the redistribution of matter on small scales, as illustrated in Fig. 3. The contraction of the high-density regions is visible in Fig. 17 by Tempel et al. (2009), which shows the changes of the sizes of particle samples, giving rise to the present-day clusters of galaxies. In central regions of superclusters clusters formed by merging of a large number of primordial clusters, collected from an approximately spherical volume of outer radius about 8 h^{-1} Mpc. The lower the global density, the

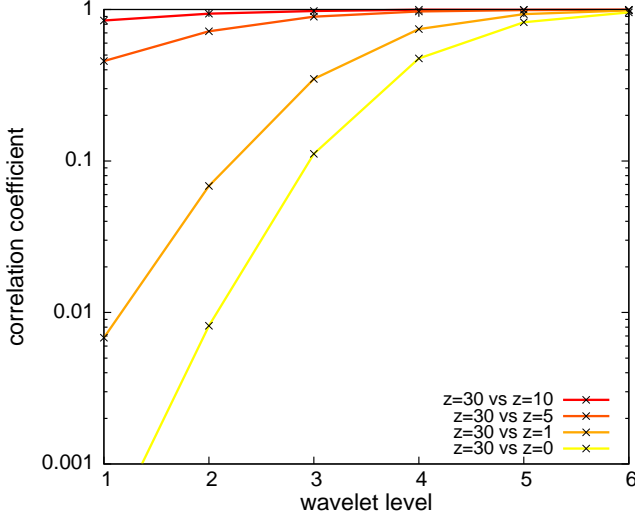


Fig. 4. Behaviour of the correlation coefficient for different redshift pairs $(z_i, z_j) \in \{(30, 10); (30, 5); (30, 1); (30, 0)\}$ for all six wavelet levels. We see that for the largest smoothing scale, i.e. w_6 , all the correlators stay very close to $r = 1$. At lower wavelet levels, as the redshift drops below $z = 30$, the lines start to deviate from $r = 1$. Thus, on the largest scales the information is approximately preserved, while on the smallest scales the information is gradually erased.

smaller is the radius of the sphere from which present clusters are formed.

2.4. The comparison of evolution of density waves of various wavelengths

Now we compare the evolution of density waves of different wavelengths, using the wavelet decomposition of our model density fields at various epochs.

A look at Fig. 2 shows that at all redshifts high-density peaks of wavelets of *medium and large* scales almost coincide. In wavelets of smaller scales, there is sometimes more than one peak in the high-density region of the next larger scale, but at least one peak is present there in practically all cases. In other words, wavelets of various scales have a tendency of phase coupling or synchronisation in peak positions. Positions of high-density peaks of wavelets w_1 and w_2 coincide for any fixed redshifts (not shown in Figs. 1 and 2, but seen in original wavelet figures). The highest of these small size density peaks also coincides in position with peaks of higher level wavelets. We conclude that the growth of small-scale peaks is amplified in high-density regions of large waves: peaks in w_4 to w_6 in Fig. 2 and peaks of wavelets of various scale in Fig. 7 of Einasto et al. (2011). This amplification of density peaks of perturbations of various scales near peak positions is the reason for wave coupling (synchronisation).

The general conclusion from the wavelet analysis of all scales and from the comparison with corresponding density fields is that the synchronisation of peak positions of wavelets of *various scales* represents a general property of the evolution of the density field of the Universe. A quantitative analysis of this effect is given in the next section.

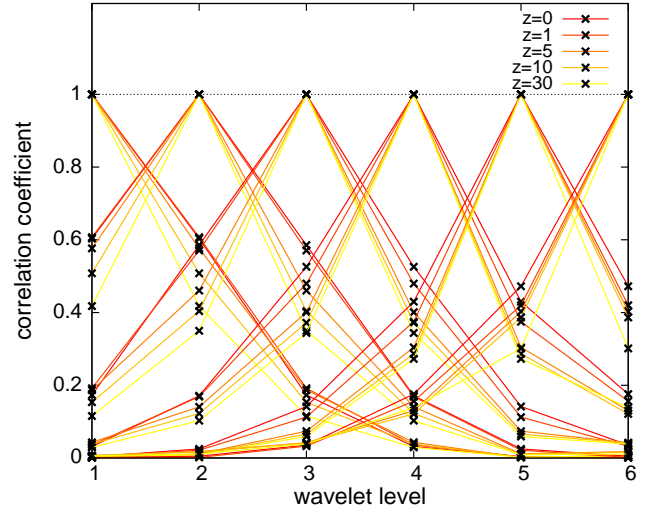


Fig. 5. Correlators at fixed redshifts $z_i = z_j = 0, 1, 5, 10, 30$ from top to bottom (from red to yellow) for high-density regions. Note that in this figure we define the high-density regions as the ones where the pixel values on the largest smoothed wavelet field reach the top 10% of all the values. Using these pixels, we define the mask, which is used for correlating only the highest density pixels with the corresponding values smoothed on a smaller scale.

3. Correlation analysis of wavelet-decomposed density fields

In this section we attempt to quantify some of the qualitative statements given above. To this end we perform the correlation analysis of wavelet-decomposed density fields. For clarity we will use only the model M256 because the other ones lead to very similar results. Here we have six wavelet levels: w_1, w_2, \dots, w_6 with the upper smoothing scales of $4, 8, \dots, 128 h^{-1}$ Mpc, respectively. We use the simulated density fields at five different redshifts: $z = 30, 10, 5, 1, 0$.

Most generally, we have chosen two redshifts, z_i and z_j , along with two wavelet levels, w_m and w_n , and calculated the following correlators:

$$r_{w_m z_i, w_n z_j} = \frac{\langle \delta_{w_m z_i} \delta_{w_n z_j} \rangle}{\sqrt{\langle \delta_{w_m z_i}^2 \rangle \langle \delta_{w_n z_j}^2 \rangle}}. \quad (1)$$

Here $\delta_{w_m z_i}$ corresponds to the wavelet-decomposed density field for level w_m at redshift z_i . The angle brackets represent ensemble average, which under the ergodicity assumption is replaced by a simple spatial average. Note that all wavelet-filtered fields have zero mean, i.e. $\langle \delta_{w_m z_i} \rangle = 0$. Also note that we calculate the correlators for zero lag only, i.e., we do not shift one field with respect to the other one. In the following we will use two types of correlators:

1. Fixed wavelet scale correlators, i.e., $w_m = w_n$, at different redshifts.
2. Correlators at fixed redshifts, i.e., $z_i = z_j$, for different wavelet levels.

In the first case we take one of the density fields always at redshift $z = 30$, which is high enough for all the scales of interest to be well in the linear regime. It is easy to understand that under the linear evolution, where the values of the density contrast δ get

just multiplied by the same scale-independent but time-varying factor, the correlation coefficient should always stay at the value $r = 1$, i.e., all the initial information is well preserved. In Fig. 4 we show the behaviour of the correlation coefficient for different redshift pairs: $(z_i, z_j) \in \{(30, 10); (30, 5); (30, 1); (30, 0)\}$ for all the six wavelet levels. It is easy to see that for the largest smoothing scale, i.e., w_6 , all the correlators stay very close to $r = 1$, while later on, as the other redshift drops below than $z = 30$, the lines start to decline from $r = 1$, especially at the smallest scales. Thus, on the largest scales the information is approximately conserved, while on the smallest scales the information gets erased. The lower the redshift of the other density field, the higher the effect of the information erasure. In practice, for the cases $z = 10$ and $z = 5$ the loss of information is relatively modest for all wavelet levels. For $z = 1$ and $z = 0$ the information is approximately preserved if the wavelet level $w \geq 4$.

In Fig. 5 we plot the correlators at fixed redshifts $z_i = z_j = 0, 1, 5, 10, 30$ from top to bottom (from red to yellow). For $w_m = 1$ the curves are peaked at $w_n = 1$, while they gradually drop as w_n is increased to higher values. Similarly, the curves for $w_m = 2$ are peaked at $w_n = 2$, and get reduced as the distance increases from this point. For the other w_n values the behaviour is very similar. As long as the evolution proceeds in a linear manner, i.e., the growth depends only on redshift, but is independent of the wavelet scale, the coupling kernels plotted in Fig. 5 should stay exactly the same. However, we see that the lower the output redshift, the broader are the coupling kernels, i.e., a nonlinear evolution in general leads to the additional coupling of the nearby wavelet modes. Also, note that in this figure we define the high-density regions as the ones where the pixel values on the largest scale wavelet field reach to the top 10% of the values. Using these pixels we define the mask, which is used for correlating only the highest 10% of the density values with the corresponding values smoothed density on the smaller scale. Thus, in this case we have looked only how the highest density regions correlate with each other. We note that owing to nonlinear evolution, the coupling kernels become broader and broader with time. It is important to realise that even for the linear evolution of the Gaussian density field the nearby wavelet levels at fixed redshift are significantly coupled, because in this case the neighbouring levels tend to contain some of the common Fourier space modes. Assuming only the linear evolution, clearly the coupling does not change with redshift.

4. Wavelet analysis of the SDSS luminosity density field

4.1. The SDSS luminosity density field

The luminosity density field was calculated using galaxy data of the Main sample of the contiguous Northern area of the SDSS data release 7 (DR7) (Abazajian et al. 2009). The DR7 sample has, after applying extinction corrections, Petrosian r -magnitude limits, $14.5 \leq r \leq 17.77$. We used for this analysis galaxies in the redshift interval $2700 \leq cz \leq 60000 \text{ km s}^{-1}$. The SDSS data reduction procedure consists of two steps: (1) the calculation of the distance, the absolute magnitude, and the weight factor for each galaxy of the sample, and (2) the calculation of the luminosity density field using an appropriate kernel and a chosen smoothing length. We estimated total luminosities of groups and isolated galaxies in our flux-limited sample, using weights of galaxies that take into account galaxies and galaxy groups too faint to fall into the observational window of absolute magnitudes at the distance of the galaxy. When calculating luminosities of galaxies

we regard every galaxy as a visible member of a group within the visible range of absolute magnitudes. For details of the calculation of the luminosity density field see Appendix A.1. A supercluster catalogue based on the luminosity density field of SDSS DR7 is published by Liivamägi et al. (2010), and the luminosity function of galaxies by Tempel et al. (2011).

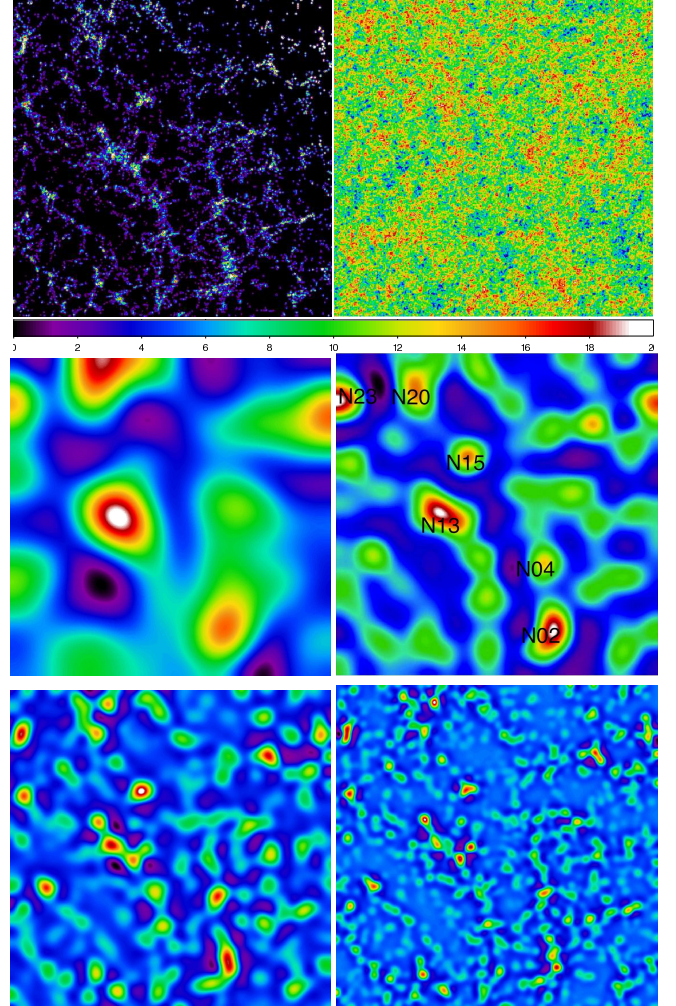


Fig. 6. Upper left panel shows a two-dimensional rectangular region of size 512×512 Mpc (using Hubble constant $h = 0.8$), extracted from the high-resolution luminosity density field of the Northern equatorial wedge of the SDSS. The density was calculated using Gaussian smoothing with the rms scale 0.8 Mpc. The observer is located at the lower left corner. Colour-coded density levels used in plotting are in the interval from 0 to 10 in mean density units with the highest value corresponding to the white colour, using the SAOImage program DS9 colour palette SLS. The upper right panel shows the same density field as in the previous panel, but the phases randomly shifted. With shifting the phases of density waves some densities become negative, thus in this case colour codes are in the density interval ± 3.5 . Middle and lower panels show the wavelets w_7 , w_6 , w_5 , and w_4 of the wedge. The middle left panel shows density waves of scales approximately equal to half of the box size, each following panel shows waves with half the length. Wavelet densities used in plotting have both negative and positive values, i.e., they correspond to under- and over-densities of matter, colour coding is linear. Supercluster numbers according to the catalogue by Einasto et al. (2003) are shown in the middle right panel w_6 .

For the present wavelet analysis we used the Northern equatorial wedge of 2.5 degrees thickness up to redshift $z = 0.2$, see Fig. 6². The high-resolution projected two-dimensional luminosity density field was found using Gaussian smoothing with scale 0.8 Mpc. Densities were found in a grid of bin size 1 Mpc. To reduce the wedge to unit thickness, density values were divided by the ratio of the thickness of the wedge at a particular distance from the observer, and at the mean distance. We use a rectangular sub-region of the field suitable for the Fourier and wavelet analysis.

4.2. Fourier and wavelet decomposition of the SDSS density field

The importance of the phase information in the cosmic web formation has been understood long ago, as demonstrated by Coles & Chiang (2000) by randomising phases of a simulated filamentary network. To study the role of phase information in more detail, we extracted a rectangular region with the box size 512 Mpc, calculated for the Hubble constant $h = 0.8$, from the density field of the SDSS Northern equatorial slice. This region is shown in the upper left panel of Fig. 6. We Fourier-transformed the 2D density field and randomised phases of all Fourier components, and thereafter Fourier-transformed it back to see the resulting density field. A similar procedure has been applied also by Coles & Chiang (2000). The modified field has the same amplitudes of all wave-numbers k as the original field, only the phases of waves are different. Results are shown in the right upper panel of Fig. 6. We see that the whole structure of superclusters, filaments and voids has gone, the field is fully covered by tiny randomly spaced density enhancements. There are no clusters of galaxies in this picture, comparable in the luminosity to real clusters of galaxies. Fourier phase randomising in numerical models by Chiang & Coles (2000) and Coles & Chiang (2000) shows similar results.

This simple example shows the importance of the density perturbation phases in the cosmic web formation.

4.3. Phase synchronisation and the supercluster structure

Next we use the wavelet analysis to investigate the role of density waves of different scales. Figure 6 shows wavelets 7 to 4 of the Northern rectangular region. These wavelets characterise waves of length about 256, 128, 64, and 32 Mpc, respectively (note that all scales in the Figure 6 are given using Hubble constant $h = 0.8$). In wavelet figures both under- and over-densities are shown. Extreme levels were chosen so that main features of the structure are well visible.

The middle left panel of Fig. 6 shows the waves of length about 256 Mpc. In its highest density regions there are three very rich superclusters: N20 from the list by Einasto et al. (2003), located in the upper part of the figure, supercluster N13 (SCL126 from the list by Einasto et al. (2001) in the Sloan Great Wall) near the centre, and supercluster N02 (SCL82) in the lower right part of the panel.

The next panel shows waves of scales about 128 Mpc. Here the most prominent features are superclusters N13 (SCL126) and N02 (SCL82), also the supercluster N23 (SCL155) in the upper left part of the panel is fairly strong, seen as a weak density peak already in the previous panel. In addition we see the supercluster N15 just above N13 near the minimum of the wave of 256 Mpc

scale, and a number of poorer superclusters located mostly in voids defined by waves of larger size.

The lower left panel plots waves of scales about 64 Mpc. Here all superclusters seen on larger scales are also visible. A large fraction of density enhancements are either situated just in the middle of low-density regions of the previous panel, or they divide massive superclusters into smaller subunits. This property is repeated in the next panel. Here the highest peaks are substructures of rich superclusters, and there are numerous smaller density enhancements (clusters) between the peaks of the previous panel.

When we compare the density waves of all scales, we arrive at the conclusion that superclusters form in regions where density waves of medium and large scales combine in *similar over-density phases*. The larger the scale of the wave where this coincidence takes place, the richer the supercluster.

Similarly, voids form in regions where density waves of medium and large scales combine in *similar under-density phases*. In large voids medium-scale perturbations generate a web of filamentary structures with knots; for a description of the formation of such a web see Bond et al. (1996). The influence of density perturbations of various scales on the cosmic web formation is discussed in more detail by Suhhonenko et al. (2011).

This simple analysis very clearly demonstrates the role of phase coupling (synchronisation) of density waves of different scales in the formation of the supercluster-void network. A wavelet analysis of the full SDSS DR7 contiguous Northern region is in progress, results will be published in a separate paper.

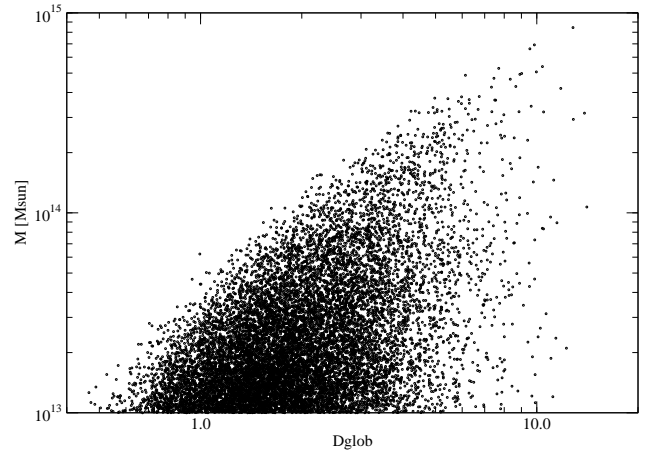


Fig. 7. DF cluster masses of the model L256 as a function of the global density. Masses are given in solar units, densities in units of the mean density of the model.

5. Discussion

5.1. The role of phase synchronisation in the formation of clusters and superclusters

The wavelet decomposition of SDSS data has shown that superclusters form in regions where density waves of medium and large scales combine in similar over-density phases. Now we shall consider the role of phase synchronisation in the formation of galaxy clusters.

Our previous analysis has shown that clusters of galaxies (haloes in simulations) form in places where small density waves

² This wavelet decomposition was first presented by Einasto (2006b).

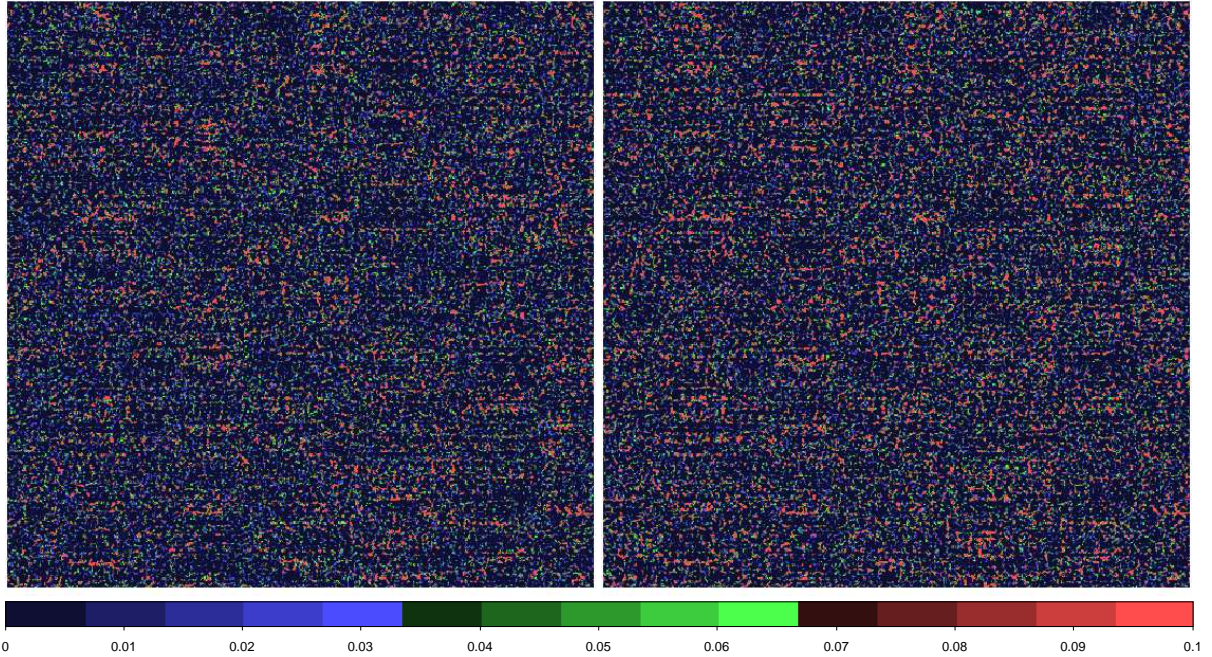


Fig. 8. Wavelets w_1 of models L256.256 and L256.008 at redshift $z = 30$ are shown in the left and right panel, respectively, at coordinate $k = 1$. Densities are expressed in linear scale, only over-density regions are shown.

in a certain range of scales combine in similar over-density regions of waves. This is clearly seen as high level correlations of wavelets of levels 1, 2, and 3 in Fig. 5, and close positions of maxima of wavelets w_4 and w_5 , and positions of rich clusters in the high-resolution density field in Fig. 6.

To see the role of phase synchronisation in the formation of clusters we shall use the density field (DF) clusters of the simulation of box length $L = 256 h^{-1}$ Mpc with resolution 512^3 particles and cells, the model L256. We define DF clusters as peaks of the high-resolution density field, calculated with the kernel of radius equal to the cell size of the simulation, the field D_0 (see Appendix A.3). DF cluster positions were identified as grid coordinates i, j, k of the local maxima of the field D_0 . The mass of the DF clusters, M_{cl} , was found by counting local density values in cells within ± 4 cells from the central one, i.e., within a box of half-length $2.5 h^{-1}$ Mpc, centred on the peak. We express DF cluster masses in solar units using the masses of particles. This sample of DF clusters was used by Suhhonenko et al. (2011) to find DF cluster mass distribution and cluster-defined void radii. To investigate the growth of structures in the standard Λ CDM cosmogony, Ludlow & Porciani (2010) used a slightly different algorithm to find density peaks in simulations.

The relationship between DF cluster masses and global densities is shown in Fig. 7. Global densities at the peak positions were found using the density field calculated with a kernel of radius $8 h^{-1}$ Mpc, the field D_4 . The figure shows that there is an upper limit of masses of DF clusters for any given global density value. Global densities calculated with a kernel of radius $8 h^{-1}$ Mpc were used to define superclusters (Einasto et al. 2003, 2006, 2007; Liivamägi et al. 2010), using a density threshold ≈ 4.5 in mean density units. We see that most massive DF clusters are located in superclusters. As the global density decreases, the upper mass limit of DF clusters also decreases. A similar tendency is found in SDSS clusters of galaxies by Einasto et al. (2005): in high-density environment clusters have a mean luminosity a factor of ≈ 5 higher than in a low-density environment.

This is the result of phase synchronisation: the larger the scale of density waves, where the maxima of waves of different scales have close positions, the larger are the masses of DF clusters. This also explains why there are no very rich clusters in a low-density environment: amplification by large-scale density waves is needed to form a very massive cluster. This amplification occurs only in the regions we call superclusters, as seen also in the SDSS data in Fig. 6.

Figure 7 shows that at any given global density value there is a large range of masses of DF clusters. This has a simple explanation. Small-mass DF clusters are located far from the maxima of large-scale waves, seen in wavelets of higher order.

We conclude that in the formation of both small and large systems of galaxies the synchronisation of phases of density waves of different scales plays an important role. Our experience shows that the wavelet analysis has a good diagnostic value in understanding the evolution of systems of galaxies of different richness.

5.2. Phase synchronisation as a physical process

Phase synchronisation between different scales is a physical process that requires a causal connection between different points in space. Because standard inflation provides us with this connection for scales up to very large ones, much exceeding the present Hubble scale, this synchronisation can already be imprinted into the initial spectrum – actually, this is the standard modern paradigm. However, it has not yet been proved if this initial synchronisation under the assumption of Gaussian statistics of perturbations in the linear regime is sufficient for the complete explanation of the structure and evolution of the cosmic web. Thus, our investigation may also shed light on the actual statistics of the primordial spectrum including its behaviour at large deviations from rms values. An alternative possibility might be some physical hydrodynamical processes acting before and during recombina-

tion. However, scales larger than the sound horizon at recombination, ≈ 146 Mpc according to the most recent cosmological data by Jarosik et al. (2010) remain unaffected by any such process.

Finally, larger scales may affect the evolution of smaller ones in the recent epoch. It is well known that density perturbations of large scales evolve almost linearly and do not change their positions. This behaviour was used by Kofman & Shandarin (1988) in the adhesion theory of the evolution of the large-scale structure of the Universe. Applying Burgers equations, these authors predicted the actual geometrical structure of the cosmic web skeleton, using the primordial (post-inflation) gravitation potential field. Numerical simulations with the same initial conditions confirmed the correctness of the prediction. This calculation shows that the cosmic web skeleton was created at a very early stage of the evolution of the Universe. Our analysis has shown how this stability of the shape of the cosmic web skeleton is expressed in wavelet terms.

To understand better the synchronisation of waves of different scales as a physical process, we used two models of the L256 series. The first model has a full power spectrum, the model L256.256. The other model has a power spectrum truncated at wave-number k_t , so that the amplitude of the power spectrum on large scales is zero: $P(k) = 0$, if $k < k_t$, wavelength $\lambda_t = 2\pi/k_t = 8 h^{-1}$ Mpc, the model L256.008. Data of these simulations are described by Suhhonenko et al. (2011).

The power spectrum of density perturbations has the highest power at small scales. Accordingly, the influence of small-scale perturbations relative to large-scale perturbations is strongest in the early period of structure evolution. For this reason the density fields and wavelets w_1 at early epochs are almost identical for the full model L256.256, and for the model cut at small scales, $\lambda_t = 8 h^{-1}$ Mpc, L256.008, see Fig. 8. Eventually, perturbations of larger scale start to affect the evolution. These perturbations amplify small-scale perturbations near maxima, and suppress small-scale perturbations near minima. In this way the growth of small-scale perturbations becomes non-linear. Thereafter still larger perturbations amplify smaller perturbation near their maxima, and suppress smaller perturbations near their minima, and so on. The largest amplification (non-linearity) occurs in regions where maxima of perturbations of all scales happen to coincide. In such a way the synchronisation of phases of waves of different scales occurs as a natural process. The synchronisation of waves of different scales as a function of redshift z is seen graphically in Fig. 7 of Einasto et al. (2011).

6. Conclusions

Main conclusions of the present paper can be formulated as follows.

1. The wavelet analysis has demonstrated a good diagnostic value for studying the evolution of galaxy systems of various scales and masses.
2. In the formation of cosmic structures the synchronisation (coupling) of density waves of different scales plays an important role.
3. Positions of density maxima of waves of large and medium scales practically do not change during the evolution. On smaller scales positions of density maxima change during the evolution, the changes are larger for waves with shorter wavelengths.

4. Superclusters are objects where density waves of medium and large scales combine *in similar phases to generate high-density regions*.
5. Voids are regions in space where density waves of medium and large scales combine *in similar under-density phases*.
6. Clusters of galaxies are objects where density waves of small scales combine in similar over-density phases.
7. The larger is the scale of the highest phase synchronisation, the richer are the clusters and superclusters.

Acknowledgements. We thank the referee for a constructive report that helped to improve the paper. The present study was supported by the Estonian Science Foundation grants No. 7146, and 8005, and by the Estonian Ministry for Education and Science grant SF0060067s08. It has also been supported by ICRAnet through a professorship for Jaan Einasto, and by the University of Valencia (Vicerrectorado de Investigación) through a visiting professorship for Enn Saar and by the Spanish MEC projects “ALHAMBRA” (AYA2006-14056) and “PAU” (CSD2007-00060), including FEDER contributions. J.E., I.S. and E.T. thank Leibniz-Institut für Astrophysik Potsdam (using DFG-grant Mu 1020/15-1), where part of this study was performed. J.E. thanks also the Aspen Center for Physics and the Johns Hopkins University for hospitality where this project was started and continued. The simulation for the model L256 was calculated at the High Performance Computing Centre, University of Tartu. For plotting the density fields and wavelets we used the SAOImage DS9 program. A.A.S. acknowledges the RESCEU hospitality as a visiting professor. He was also partially supported by the Russian Foundation for Basic Research grant No. 11-02-00643 and by the Scientific Programme “Astronomy” of the Russian Academy of Sciences.

We thank the SDSS Team for the publicly available data releases. Funding for the SDSS and SDSS-II has been provided by the Alfred P. Sloan Foundation, the Participating Institutions, the National Science Foundation, the U.S. Department of Energy, the National Aeronautics and Space Administration, the Japanese Monbukagakusho, the Max Planck Society, and the Higher Education Funding Council for England. The SDSS Web Site is <http://www.sdss.org/>.

The SDSS is managed by the Astrophysical Research Consortium for the Participating Institutions. The Participating Institutions are the American Museum of Natural History, Astrophysical Institute Potsdam, University of Basel, University of Cambridge, Case Western Reserve University, University of Chicago, Drexel University, Fermilab, the Institute for Advanced Study, the Japan Participation Group, Johns Hopkins University, the Joint Institute for Nuclear Astrophysics, the Kavli Institute for Particle Astrophysics and Cosmology, the Korean Scientist Group, the Chinese Academy of Sciences (LAMOST), Los Alamos National Laboratory, the Max-Planck-Institute for Astronomy (MPIA), the Max-Planck-Institute for Astrophysics (MPA), New Mexico State University, Ohio State University, University of Pittsburgh, University of Portsmouth, Princeton University, the United States Naval Observatory, and the University of Washington.

Appendix A: Density field and wavelets

A.1. Density field

To estimate the expected total luminosity of groups or single galaxies, we assume that the luminosity functions derived for a representative volume can be applied also to individual groups and galaxies. Under this assumption the estimated total luminosity per one visible galaxy is

$$L_{\text{tot}} = L_{\text{obs}} W_d, \quad (\text{A.1})$$

where $L_{\text{obs}} = L_{\odot} 10^{0.4 \times (M_{\odot} - M)}$ is the luminosity of the visible galaxy of absolute magnitude M (in units of the luminosity of the Sun, L_{\odot}), and

$$W_d = \frac{\int_0^{\infty} L F(L) dL}{\int_{L_1}^{L_2} L F(L) dL} \quad (\text{A.2})$$

is the luminous-density weight (the ratio of the expected total luminosity to the expected luminosity in the visibility window). L_1 and L_2 are lower and upper limit of the luminosity window,

respectively. In our calculations we adopted the absolute magnitude of the Sun in the r filter $M_{\odot} = 4.64$ (Blanton & Roweis 2007).

The k -correction for the SDSS galaxies is calculated using the KCORRECT algorithm (version v4.1.4) developed by Blanton et al. (2003b) and Blanton & Roweis (2007). Evolution correction e has been calculated according to Blanton et al. (2003a). For details of the data reduction procedure see Tago et al. (2010).

In calculating of the total expected luminosity we used a double-power-law luminosity function with a smooth transition:

$$\phi(L)dL \propto (L/L^*)^{\alpha}(1 + (L/L^*)^{\gamma})^{(\delta-\alpha)/\gamma}d(L/L^*), \quad (\text{A.3})$$

where α is the exponent at low luminosities ($L/L^* \ll 1$), δ is the exponent at high luminosities ($L/L^* \gg 1$), γ is a parameter that determines the speed of transition between the two power laws, and L^* is the characteristic luminosity of the transition, similar to the characteristic luminosity of the Schechter function. As demonstrated by Tempel et al. (2009), the double-power-law luminosity function fits observed luminosity distribution of galaxies and groups of galaxies better than the Schechter function, in particular in the high-luminosity end of the distribution.

A.2. Kernel method

To calculate a density field, we need to convert the spatial positions of galaxies \mathbf{r}_i and their luminosities L_i into spatial (luminosity) densities. The standard approach is to use kernel densities

$$\rho(\mathbf{r}) = \sum_i K(\mathbf{r} - \mathbf{r}_i; a) L_i, \quad (\text{A.4})$$

where the sum is over all galaxies, and $K(\mathbf{r}; a)$ is a kernel function of a width a . Good kernels for calculating densities on a spatial grid are generated by box splines B_J . Box splines are local and they are interpolating on a grid:

$$\sum_i B_J(x - i) = 1, \quad (\text{A.5})$$

for any x and a small number of indices that give non-zero values for $B_J(x)$.

We use the popular B_3 spline function:

$$B_3(x) = \frac{1}{12} \left[|x - 2|^3 - 4|x - 1|^3 + 6|x|^3 - 4|x + 1|^3 + |x + 2|^3 \right]. \quad (\text{A.6})$$

We define the (one-dimensional) B_3 box spline kernel $K_B^{(1)}$ of the width a as

$$K_B^{(1)}(x; a, \delta) = B_3(x/a)(\delta/a), \quad (\text{A.7})$$

where δ is the grid step. This kernel differs from zero only in the interval $x \in [-2a, 2a]$; it is close to a Gaussian with $\sigma = 1$ in the region $x \in [-a, a]$, so its effective width is $2a$ (see, e.g., Saar 2009).

The kernel preserves the interpolation property exactly for all values of a and δ , where the ratio a/δ is an integer. (This kernel can be used also if this ratio is not an integer, and $a \gg \delta$; the kernel sums to 1 in this case, too, with a very small error). This means that if we apply this kernel to N points on a one-dimensional grid, the sum of the densities over the grid is exactly N .

The three-dimensional kernel $K_B^{(3)}$ is given by the direct product of three one-dimensional kernels:

$$K_B^{(3)}(\mathbf{r}; a, \delta) \equiv K_B^{(1)}(x; a, \delta)K_B^{(1)}(y; a, \delta)K_B^{(1)}(z; a, \delta), \quad (\text{A.8})$$

where $\mathbf{r} \equiv \{x, y, z\}$. Although this is a direct product, it is isotropic to a good degree (Saar 2009).

To calculate the high-resolution density field, we use the kernel of a scale equal to the cell size of the simulation, $l_c = L_b/N_{\text{grid}}$, where L_b is the size of the simulation box, and N_{grid} is the number of grid elements in one coordinate.

A.3. Wavelets

We use the 'à trous' wavelet transform (Martínez & Saar 2002). The algorithm of the wavelet transform works as follows. Let us have a data set D (particles in simulations or luminosity weighted galaxies in SDSS data), located in a box of size $n \times n \times n$. The wavelet transform decomposes the data set as a superposition of the form

$$D = D_J + \sum_{j=1}^J w_j, \quad (\text{A.9})$$

where D_J is the smoothed version of the original data D , and w_j represents the structure of D at scale 2^j , (see Starck et al. 1998; Starck & Murtagh 2002). The wavelet decomposition output is J three-dimensional density fields D_j and wavelets w_j of size $n \times n \times n$. Following the traditional indexing convention, we denote density fields and wavelets of the finest scale as $j = 1$. All density fields were calculated with the B_3 spline kernel. The smoothed version of the original data, $D_J = D_0$, is the density field found with the kernel of the scale, equal to the cell size of the simulation l_c .

We calculated wavelets of index j by subtraction of density fields:

$$w_j = D_{j-1} - D_j, \quad (\text{A.10})$$

where every higher level density field D_j was calculated with kernel size twice larger than the previous level field D_{j-1} . In such construction a wavelet of index j corresponds to density waves between scales $\Delta_{j-1} = l_c \times 2^{j-1/2}$ and $\Delta_j = l_c \times 2^{j+1/2}$, i.e., diameters of kernels used in calculation of density fields D_{j-1} and D_j .

References

- Abazajian, K. N., Adelman-McCarthy, J. K., Agüeros, M. A., et al. 2009, ApJS, 182, 543
 Albrecht, A. & Steinhardt, P. J. 1982, Physical Review Letters, 48, 1220
 Bertschinger, E. 1995, ArXiv:astro-ph/9506070
 Blanton, M. R., Brinkmann, J., Csabai, I., et al. 2003a, AJ, 125, 2348
 Blanton, M. R., Hogg, D. W., Bahcall, N. A., et al. 2003b, ApJ, 592, 819
 Blanton, M. R. & Roweis, S. 2007, AJ, 133, 734
 Bond, J. R., Kofman, L., & Pogosyan, D. 1996, Nature, 380, 603
 Chiang, L. & Coles, P. 2000, MNRAS, 311, 809
 Chiang, L., Coles, P., & Naselsky, P. 2002, MNRAS, 337, 488
 Coles, P. 2009, in Lecture Notes in Physics, Berlin Springer Verlag, Vol. 665, Data Analysis in Cosmology, ed. V. J. Martinez, E. Saar, E. M. Gonzales, & M. J. Pons-Borderia, 493
 Coles, P. & Chiang, L. 2000, Nature, 406, 376
 de Lapparent, V., Geller, M. J., & Huchra, J. P. 1986, ApJL, 302, L1
 Einasto, J. 2006a, Communications of the Konkoly Observatory Hungary, 104, 163
 Einasto, J. 2006b, in Bernard's Cosmic Stories: From Primordial Fluctuations to the Birth of Stars and Galaxies
 Einasto, J. 2009, arXiv:0906.5272

- Einasto, J., Einasto, M., Saar, E., et al. 2006, *A&A*, 459, L1
- Einasto, J., Einasto, M., Tago, E., et al. 2007, *A&A*, 462, 811
- Einasto, J., Hütsi, G., Einasto, M., et al. 2003, *A&A*, 405, 425
- Einasto, J., Jõeveer, M., & Saar, E. 1980, *MNRAS*, 193, 353
- Einasto, J., Suhhonenko, I., Hütsi, G., et al. 2011, arXiv:1105.2464
- Einasto, J., Tago, E., Einasto, M., et al. 2005, *A&A*, 439, 45
- Einasto, M., Einasto, J., Tago, E., Müller, V., & Andernach, H. 2001, *AJ*, 122, 2222
- Guth, A. H. 1981, *Phys. Rev. D*, 23, 347
- Guth, A. H. & Pi, S. 1982, *Physical Review Letters*, 49, 1110
- Hawking, S. W. 1982, *Physics Letters B*, 115, 295
- Hikage, C., Matsubara, T., Suto, Y., et al. 2005, *PASJ*, 57, 709
- Jarosik, N., Bennett, C. L., Dunkley, J., et al. 2010, arXiv:1001.4744
- Jones, B. J. T. 2009, in *Lecture Notes in Physics*, Berlin Springer Verlag, Vol. 665, *Data Analysis in Cosmology*, ed. V. J. Martínez, E. Saar, E. M. Gonzales, & M. J. Pons-Borderia, 3–50
- Knebe, A., Green, A., & Binney, J. 2001, *MNRAS*, 325, 845
- Kofman, L. A. & Shandarin, S. F. 1988, *Nature*, 334, 129
- Liivamägi, L. J., Tempel, E., & Saar, E. 2010, arXiv:1012.1989
- Linde, A. D. 1982, *Physics Letters B*, 108, 389
- Ludlow, A. D. & Porciani, C. 2010, arXiv:1011.2493
- Martínez, V. J. & Saar, E. 2002, *Statistics of the Galaxy Distribution* (Chapman & Hall/CRC)
- Martínez, V. J., Starck, J., Saar, E., et al. 2005, *ApJ*, 634, 744
- Mukhanov, V. F. & Chibisov, G. V. 1981, *Soviet Journal of Experimental and Theoretical Physics Letters*, 33, 532
- Romeo, A. B., Agertz, O., Moore, B., & Stadel, J. 2008, *ApJ*, 686, 1
- Ryden, B. S. & Gramann, M. 1991, *ApJL*, 383, L33
- Saar, E. 2009, in *Lecture Notes in Physics*, Berlin Springer Verlag, Vol. 665, *Data Analysis in Cosmology*, ed. V. J. Martínez, E. Saar, E. M. Gonzales, & M. J. Pons-Borderia, 523–563
- Slezak, E., de Lapparent, V., & Bijaoui, A. 1993, *ApJ*, 409, 517
- Springel, V. 2005, *MNRAS*, 364, 1105
- Starck, J. & Murtagh, F. 2002, *Astronomical image and data analysis*, ed. Starck, J.-L. & Murtagh, F.
- Starck, J., Murtagh, F. D., & Bijaoui, A. 1998, *Image Processing and Data Analysis*, ed. Starck, J.-L., Murtagh, F. D., & Bijaoui, A.
- Starobinsky, A. A. 1979, *Soviet Journal of Experimental and Theoretical Physics Letters*, 30, 682
- Starobinsky, A. A. 1980, *Physics Letters B*, 91, 99
- Starobinsky, A. A. 1982, *Physics Letters B*, 117, 175
- Suhhonenko, I., Einasto, J., Liivamägi, L. J., et al. 2011, arXiv:1101.0123
- Tago, E., Saar, E., Tempel, E., et al. 2010, *A&A*, 514, A102
- Tempel, E., Einasto, J., Einasto, M., Saar, E., & Tago, E. 2009, *A&A*, 495, 37
- Tempel, E., Saar, E., Liivamägi, L. J., et al. 2011, *A&A*, 529, A53
- van de Weygaert, R. & Schaap, W. 2009, in *Lecture Notes in Physics*, Berlin Springer Verlag, Vol. 665, *Data Analysis in Cosmology*, ed. V. J. Martínez, E. Saar, E. Martínez-González, & M.-J. Pons-Bordería, 291–413
- Vielva, P., Martínez-González, E., & Tucci, M. 2006, *MNRAS*, 365, 891
- Zeldovich, Y. B., Einasto, J., & Shandarin, S. F. 1982, *Nature*, 300, 407